

Optimization of the Local Evanescent Array-Coupled Optoelectronic Sensing Chip for Enhanced, Portable, Real-Time Sensing

Tim A. Erickson, *Student Member, IEEE*, and Kevin L. Lear, *Member, IEEE*

Abstract—Performance of the local evanescent array coupled (LEAC) biosensor is optimized by modifying the CMOS-compatible fabrication scheme and fine-tuning waveguide parameters based on simulation results of a full-vector finite difference mode solver. To enable *in situ*, real-time detection, an index-matched upper cladding reference region is patterned onto the waveguide. The reference region is followed by a sensing region exposed to the analyte, which is delivered via a flow cell. An on-chip, continuous photodetector array is implemented, which enables the fabrication of an optically smooth lower cladding/core interface, removing the need for chemical-mechanical polishing. As close mode-matching between reference and sensing regions increases the optical power launched into the sensing region, different mixtures of oils ($n = 1.4680\text{--}1.4722$) were used as a proof of concept for real-time refractive index measurements. The $\sim 1\text{-cm}^2$ LEAC chip, which exploits three independent sensing mechanisms, is demonstrated to have a static sensitivity of 4.6×10^{-6} RIU and a real-time (2s resolution) sensitivity of 4.1×10^{-5} RIU.

Index Terms—Biosensor, evanescent wave sensor, optical waveguide, real-time sensing.

I. INTRODUCTION

OPTOELECTRONIC biosensors, which leverage existing CMOS technology, have the potential to deliver cost-effective, real-time, multi-analyte diagnostic information at the point of care. In recent years, a number of photonic sensing platforms have been realized, which take advantage of the interaction between the optical field's evanescent tail and the surrounding environment, in order to transduce a change in the optical signal. These include the ring resonators [1]–[3], SPR sensors [4]–[6], interferometric sensors [7]–[12], photonic crystal sensors [13]–[14], and fiber sensors [15]–[16]. Each of these sensing platforms can provide exquisite sensitivity, at the expense of requiring significant external hardware, including narrow linewidth lasers, optical spectrum analyzers (OSA), precise temperature control, separate optical

detectors, and/or bulky external optical components, which may be cost prohibitive [17].

The LEAC platform has shown promise as a low-cost, stand alone biosensor. The LEAC chip features an integrated photodetector, exhibits minimal temperature dependence and requires only an LED for waveguide excitation [18], and it could be readily mass-produced using existing CMOS technology. For comparison, Table I references sensors described in recent literature. It includes the sensing modality, demonstrated sensitivity (static and/or real-time) in refractive index units (RIU), as well as required major external components. Sensitivities typically range from 10^{-4} to 10^{-7} RIU. Sensors with the best sensitivity performance often require significant external hardware.

The operating principle behind the LEAC biosensor is the local evanescent field shift effect [19], whereby the guided mode in the waveguide core is shifted upward in response to an increase in the refractive index of the upper cladding sensing region. As a result of the field shift, there is less coupling between leaky modes and the underlying Si photodetector. The decrease in photodetector coupling corresponds to a decrease in the measured photocurrent. The LEAC chip has previously been demonstrated to statically detect dry films of BSA [18], mouse IgG [20], tuberculosis antibody HspX [20], and C-reactive protein [21]. In this work, we demonstrate functionalization of the LEAC biosensor for real-time refractive index sensing.

While the LEAC biosensor has been validated for static sensing of dry films, a review of the published data indicates that multiple issues need to be addressed in order to realize the full potential of the LEAC chip as a fully portable biosensing platform. Chief among these remaining challenges are improving sensitivity, enabling real-time detection, and integrating a fluid delivery system onto the chip.

In this work, we discuss significant design and fabrication changes made to the LEAC biosensing platform, which enable real-time, refractive index sensing on a CMOS-fabricated chip. Device sensitivity is simulated and optimized by using a full-vector finite difference mode solver [22]. As device sensitivity is limited by scattering losses, an analytical scattering model is also used to assist in waveguide design and understand the effects of fabrication tolerances on scattering loss. These tolerances include both dielectric film quality and waveguide sidewall roughness. A new integrated photodetector is introduced, which both eases fabrication and generates very low dark currents, producing a photocurrent to dark current ratio

Manuscript received November 9, 2012; revised January 9, 2013; accepted January 14, 2013. Date of publication January 24, 2013; date of current version April 5, 2013. This work was supported in part by the Colorado Office of Economic Development and IT. The associate editor coordinating the review of this paper and approving it for publication was Dr. Richard T. Kouzes.

T. A. Erickson is with the Electrical and Computer Engineering Department, Colorado State University, Fort Collins, CO 80523 USA (e-mail: terickso@engr.colostate.edu).

K. L. Lear is with the Electrical and Computer Engineering Department and the School of Biomedical Engineering, Colorado State University, Fort Collins, CO 80523 USA (e-mail: kevin.lear@colostate.edu).

Color versions of one or more of the figures in this paper are available online at <http://ieeexplore.ieee.org>.

Digital Object Identifier 10.1109/JSEN.2013.2242058

TABLE I
EVANESCENT WAVE BASED OPTICAL SENSORS

Sensing Modality	Static Sensitivity (RIU)	Real-Time Sensitivity (RIU)	External Components
LEAC biosensor	4.6×10^{-6}	4.1×10^{-5}	LED, 4 × 4 inch PCB board for photocurrent readout
Ring resonator [2]	no data	$\sim 10^{-5}$	Temperature-stabilized chuck, Ge photodetector
Ring resonator [3]	7.6×10^{-7}	no data	Tunable laser, OSA (0.22 pm precision), focusing optics
Fiber-based SPR [4]	7×10^{-7}	no data	Broadband light source, OSA (1 pm precision)
Long range SPR [5]	3×10^{-8}	no data	Superluminescent diode, OSA, collimating optics
Cell phone SPR [6]	2.1×10^{-6}	no data	Cell phone with front facing camera, PDMS-based optics
Mach-zehnder Int. [7]	6×10^{-5}	no data	Broadband light source, OSA (1 pm precision)
Michelson Int. [8]	5×10^{-4}	no data	Broadband light source, OSA (1 pm precision)
Mach-zehnder Int. [9]	no data	5×10^{-6}	Laser diode, lock-in amplifier, Si photodetector
3-D mach-zehnder int. [10]	10^{-4}	no data	Tunable laser, optical power meter
Mach-zehnder int. [11]	2.5×10^{-6}	no data	External CCD, phase-stabilized laser
Young int. [12]	8.5×10^{-8}	no data	Monochromatic laser, collimating optics, CCD
Photonic crystal [13]	7×10^{-5}	no data	Tunable laser, optical power meter
Photonic crystal fiber [14]	4.6×10^{-7}	no data	Supercontinuum laser, OSA (1 pm precision)
Fiber bragg grating [15]	4×10^{-5}	no data	Tunable laser (1 pm resolution), optical power meter
Fabry-perot fiber [16]	4×10^{-5}	no data	Broadband IR light source, OSA (1 pm precision)

of greater than 50 in the sensing region. The use of an on-chip reference region of known refractive index, which enables real-time sensing is discussed along with the need to mode match at the reference/sensing region boundary, in order to improve light transmission down the waveguide and take advantage of the chip's multiple sensing mechanisms. Lastly, as a proof of concept, a flow chamber is attached to chip, and real-time sensing is demonstrated. Our results indicate that design improvements give the LEAC chip a static sensitivity of 4.6×10^{-6} RIU and real-time (2 s resolution) sensitivity of 4.1×10^{-5} on a highly portable biosensing platform.

The paper is structured as follows. In Section I, the primary sensing mechanism of the chip is discussed. In Section II, the fabrication process flow and 1-D continuous photodetector array are discussed. In Section III, chip design considerations and simulation results are discussed within the context of optimizing chip sensitivity subject to fabrication tolerances. In Section IV, results from real-time sensing experiments are presented, and the chip's performance is analyzed. In Section V, the chip's fabrication-dependent limitations are briefly discussed and future improvements to the sensing platform are proposed.

II. SENSING PRINCIPLE

A. Primary Sensing Mechanism

The primary sensing mechanism of the LEAC chip is the local evanescent field shift effect [20]. Due to the nanoscale dimensions of the waveguide core in the vertical direction, coupled light is weakly confined, so there is a strong interaction between the mode's evanescent tail and the structure's upper cladding. In response to an increase in upper cladding refractive index, the evanescent field shifts up and away from the photodetector, resulting in less photodetector coupling loss and a corresponding decrease in the measured photocurrent in the underlying photodetector, which is biased at 2.5 V. This effect is illustrated in Fig. 1, which is a cross-sectional

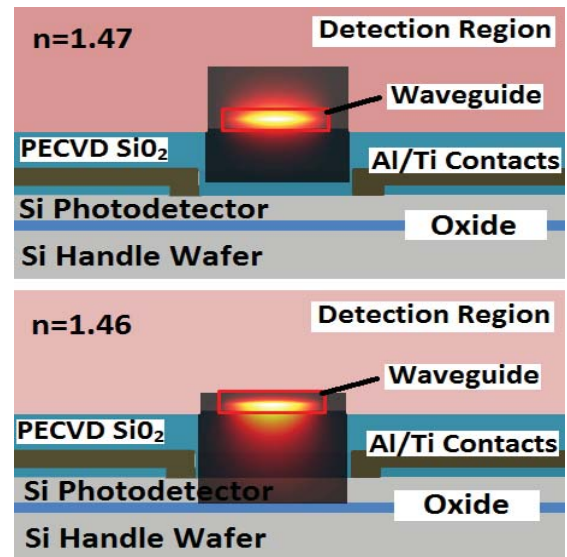


Fig. 1. Cross sectional diagram of LEAC structure, which indicates field shifting in response to changes in upper cladding index. Note that for the higher index upper cladding ($n = 1.47$), the field is shifted up and away from the underlying photodetector, whereas there is much greater field overlap with the detector for the lower index ($n = 1.46$) upper cladding.

view of the waveguide structure. Notice that the field is shifted upward and that there is minimal interaction of the evanescent field with the integrated photodetector when $n = 1.47$; however there is significant interaction when $n = 1.46$. As such, coupling to the photodetector is much higher for $n = 1.46$. For biosensing applications, analyte binding in the upper cladding sensing region would produce an increase in refractive index, so analyte binding would be transduced as a decrease in measured photocurrent.

For clarity, Figure 2 illustrates the evanescent field shift effect for upper cladding refractive indices of $n = 1.46$ and $n = 1.47$. The fields are calculated using a 2-D mode solver [22] and designate the field intensity in the

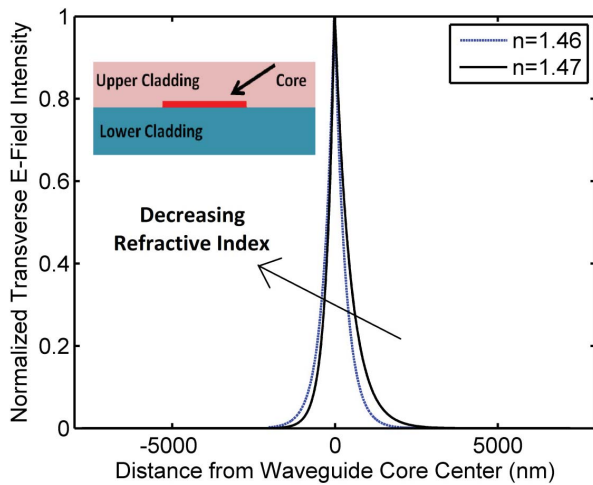


Fig. 2. Field response to $n = 1.46$ and $n = 1.47$ upper cladding refractive indices for a $7 \mu\text{m} \times 30 \text{ nm}$ SiN_x waveguide with an oxide lower cladding. Negative distance values correspond to the field below the center of the waveguide, whereas positive distance values correspond to the field above the center of the waveguide.

middle of the waveguide structure (Figure 2, inset) for the TE_{00} mode. The waveguide has a semi-infinite lower cladding ($n = 1.46$), a $30 \text{ nm} \times 7 \mu\text{m}$ SiN_x core ($n = 1.8$) and a variable index upper cladding.

III. FABRICATION AND INTEGRATED PHOTODETECTOR ARRAY

A. Device Fabrication

LEAC chips are fabricated using a simple CMOS-compatible process flow. A p-type $\langle 100 \rangle$, 100-200 ohm-cm, Silicon-On-Insulator (SOI) wafer with a $10 \mu\text{m}$ device layer (Ultrasil, Hayward, CA) is used as the starting substrate [23]. A low-temperature ($\leq 250^\circ$) process is employed, as higher temperatures significantly degrade the chip's metal-semiconductor-metal contacts by dramatically increasing dark currents in the chip's integrated photodetectors [24].

The LEAC chip's integrated photodetector structure is fabricated first, as depicted in Figs. 1 and 4. In the first step, 280 nm of SiO_2 is deposited with a PECVD system [25]. Next a window is wet etched in the oxide layer, revealing a $50 \mu\text{m} \times 6 \text{ mm}$ strip of Si. Then Ti/Al metal contacts are e-beam evaporated to partially overlap the Si, in order to create a continuous, 20-detector, 1-D photodetector array.

After fabrication of the integrated photodetector array, the waveguide sensing structure is fabricated. First, a 20 nm layer of SiN_x is deposited to form a passivation layer over the metal contacts. Then a layer of high-quality SiO_2 with a thickness t_{oxide} is PECVD-deposited to form the waveguide's lower cladding [25]. After lower cladding deposition, the waveguide core is fabricated by PECVD deposition of a thin layer of SiN_x with a thickness of t_{nitride} [26]. Standard photolithography and dry etching steps are used to form a ridge waveguide with width w and height H . The precise lower cladding oxide thickness, t_{oxide} , and waveguide core dimensions (w, t_{nitride}, H) all have a significant impact on device sensitivity, as discussed further in Waveguide Structure

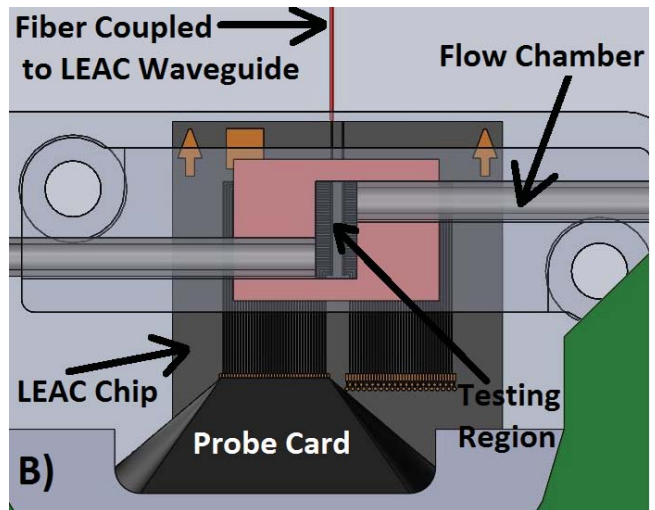
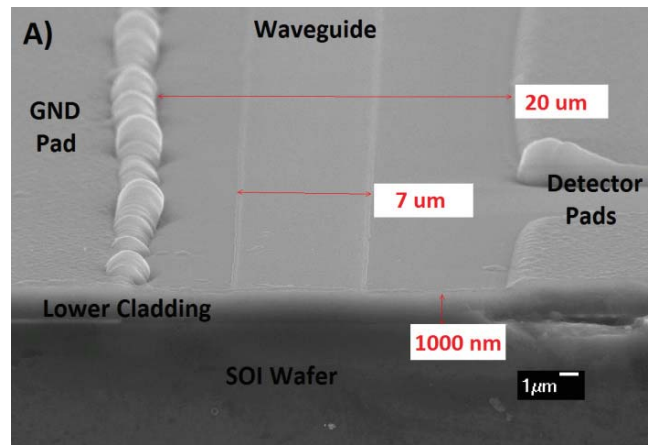


Fig. 3. (a) SEM image of LEAC structure with $7\text{-}\mu\text{m}$ -wide waveguide, and $20\text{-}\mu\text{m}$ bias-detector pad separation, and 1000 nm lower cladding. (b) Experimental setup used for experiments and prototyping. The fiber is aligned to the waveguide and fluid is syringe-injected into the flow chamber.

Optimization subsection. For reference, typical dimensions are $t_{\text{oxide}}=1000 \text{ nm}$, $t_{\text{nitride}} = H = 30 \text{ nm}$, and $w = 7 \mu\text{m}$.

In the next step of the fabrication scheme, a $2 \mu\text{m}$ thick layer of upper cladding oxide is deposited in the region of the waveguide corresponding to detectors 1–5. This step is used to establish an upper cladding reference region of known refractive index ($n = 1.458$) along the waveguide. The reference region is used to normalize for fluctuations of the coupled light intensity into the sensing region, in order to enable real-time sensing. The reference region is then followed by a sensing region. After this step, only detectors 6–10 are exposed to the analyte, as they are not covered with oxide. After reference region patterning, the edge of the chip is polished to enable end-fire coupling with a $4/125 \mu\text{m}$ fiber excited by a red laser diode centered about 650 nm . Lastly, a CNC-machined polycarbonate flow cell with a soft Viton gasket is clamped onto the chip to permit syringe-driven fluidic flow, as shown in Fig. 3b. The gasket did not leak during three rounds of identical experiments. In a commercial mass production line, an SU8 bonding technique could be readily implemented [27]. Fig. 3a is an SEM image

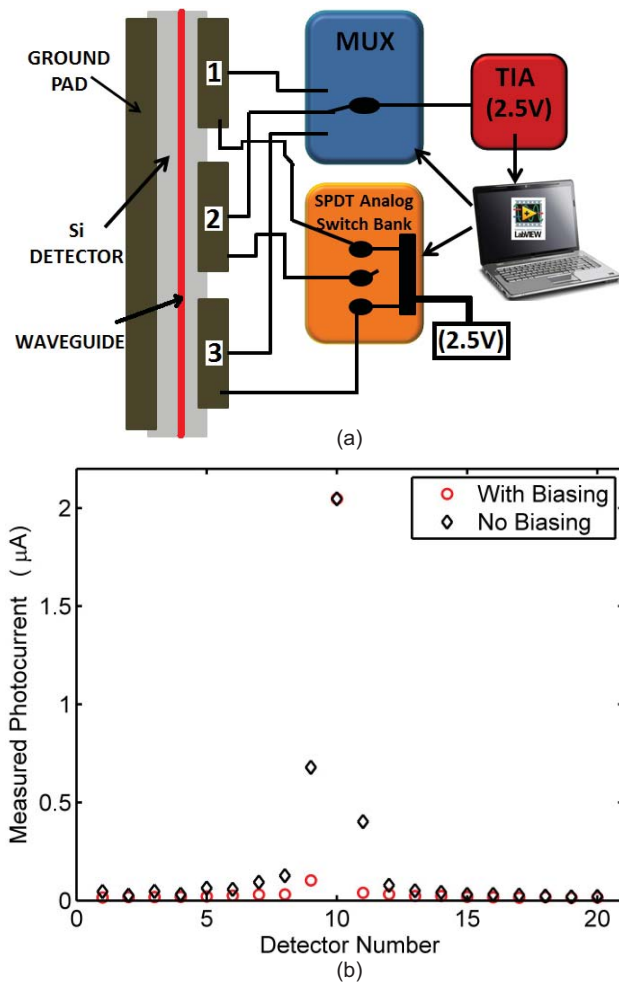


Fig. 4. (a) Diagram of continuous photodetector and biasing circuit. (b) Demonstration of photocurrent localization capabilities.

of the polished edge of the LEAC structure, which shows the optical waveguide, ground pad, and detector pads. Fig. 3b, shows the entire experimental setup, which includes the LEAC chip, integrated fluidic channel, optical fiber for waveguide excitation, and the probe card used for interfacing the chip to the photocurrent measurement circuit described in the next subsection. In a commercial fabrication process, wirebonding to a pin-grid array adapter would be used in lieu of a probe card [28].

B. Photocurrent Localization Biasing Circuit

A unique biasing circuit is employed to both accurately measure the localized photocurrent for each individual detector in the 1-D continuous photodetector array and ensure an optically smooth core/cladding interface. The ability to measure the localized photocurrent at each detector is critical, so that the local refractive index in the medium above each detector can be accurately measured. The use of the biasing circuit obviates the need for chemical mechanical polishing (CMP), an extra process step, which would be required if the detectors were etched to become electrically isolated islands [20]. Without CMP, the 1000 nm lower cladding oxide would be insufficient to planarize the gaps introduced by

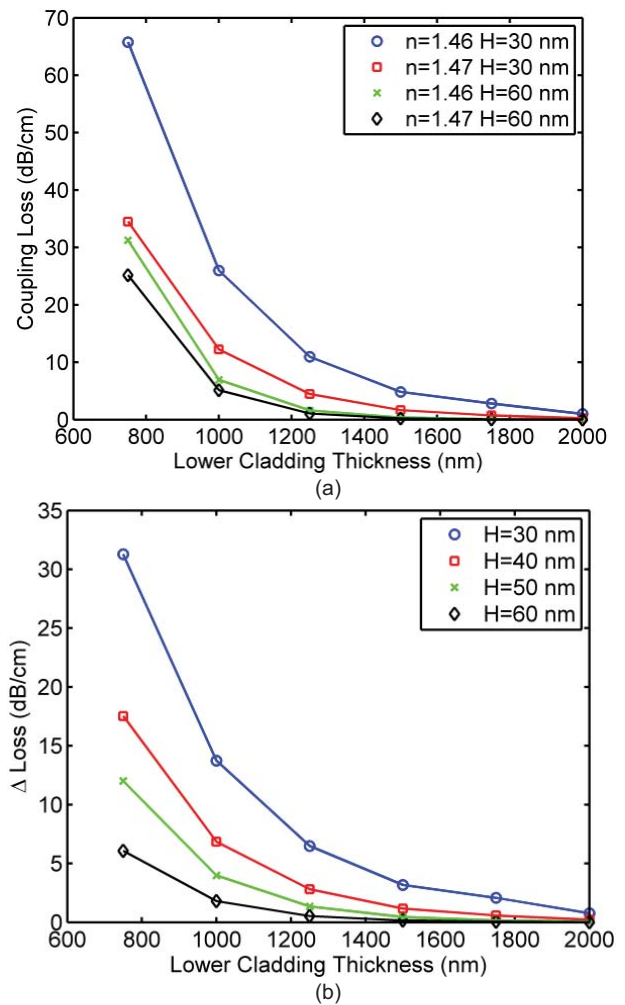


Fig. 5. (a) Coupling loss for waveguides as a function of t_{oxide} , H and upper cladding index. (b) Difference in coupling loss for an upper cladding refractive index difference of 0.01 RIU as a function of t_{oxide} and H .

etching hundreds of nanometers. Such gaps would render the waveguide inoperable due to scattering losses.

Fig. 4a shows a functional diagram of the photocurrent circuit interfaced to three representative detectors on the chip. All detector pads are held at a constant bias voltage of 2.5 V. The photocurrent localization circuit works by effectively sweeping away carriers generated in the vicinity of detectors #1 and #3, so that they are not collected by detector #2. Carriers generated in the vicinity of detector #2 are collected and converted to voltage using a 4-IC, battery-powered transimpedance amplifier (TIA) with a gain of 2 V/ μ A. The voltage output by the TIA is then output to a computer running Lab view for fully-automated data acquisition.

A simple experiment was undertaken to evaluate the performance of the biasing circuit. A single mode fiber was placed on top of individual detectors in the detector region. Fig. 4b demonstrates the photocurrent localization capabilities of the biasing circuit, when the fiber was placed directly on top of detector #10. In both cases, the direct illumination saturated #10. However, it is essential to note that the photocurrent is only well-localized when the biasing circuit is used, as

significant photocurrents are measured on adjacent detectors when the biasing circuit is turned off. This problem would only be compounded when light is coupled into the waveguide and light is present in all detector regions, further validating the need to implement the photocurrent localization biasing circuit.

IV. DEVICE OPTIMIZATION

A. Waveguide Structure Optimization Simulations

A full-vector, 2-D, finite difference modesolver [22] was used to optimize the dimensions of the waveguide in order to maximize device sensitivity. The modesolver is used to solve for leaky modes of the LEAC waveguide structure and compute substrate (photodetector) coupling losses. Simulation results indicate that device sensitivity is highly dependent on both the lower cladding ($n = 1.46$) thickness t_{oxide} and waveguide core height H . Photodetector coupling loss was computed for the fundamental TE mode for $t_{oxide} = 750, 1000, 1250, 1500, 1750,$ and 2000 nm and $H = 30, 40, 50$ and 60 nm. A guided mode was not found for cores thinner than 30 nm. All simulations were for the fundamental mode and waveguide width $w = 7 \mu\text{m}$, which was used for actual experiments.

In Fig. 5a, photodetector coupling loss is shown as a function of $t_{oxide} H$, and upper cladding index. For clarity, only waveguide heights of 30 and 60 nm are shown. As expected, photodetector coupling loss decreases as the upper cladding refractive index increases, due to the evanescent field shift effect, and photodetector coupling loss approaches zero as t_{oxide} increases. In Fig. 5b, the difference in photodetector coupling loss ($\Delta Loss$) is plotted as a function of both t_{oxide} and H for a 0.01 RIU upper cladding refractive index difference ($n = 1.46$ versus $n = 1.47$). Both parameters have a dramatic impact on device sensitivity. The difference in photodetector coupling ($\Delta Loss$) is nearly indistinguishable when $t_{oxide} = 2000$ nm and $H = 60$ nm, whereas $\Delta Loss = 31.3$ dB/cm when $t_{oxide} = 750$ and $H = 30$ nm. In general, device sensitivity is maximized by driving the waveguide closer to cutoff and reducing lower cladding thickness. However, there is a design tradeoff. As the cladding becomes thinner, photodetector coupling losses rapidly increase, which inhibits light propagation to the sensing region.

Modal simulations also indicate that mode matching, and hence index-matching at the upper cladding reference region/sensing region interface is necessary to ensure adequate light propagation down the waveguide and take advantage of another sensing mechanism. The power transmission P at each interface is computed by calculating the square of the mode overlap integral [29] (Eq. 1).

$$P = \left[\frac{\int |\mathbf{E}_1^* \mathbf{E}_2| dA}{\sqrt{\int |\mathbf{E}_1|^2 dA \int |\mathbf{E}_2|^2 dA}} \right]^2 \quad (1)$$

Fig. 6 shows the optical power transmission percentage as a function of detector region refractive index for a reference region of $n = 1.46$. Power transmission is well over 95% if the index is matched within 0.02 RIU. However, notice that for a

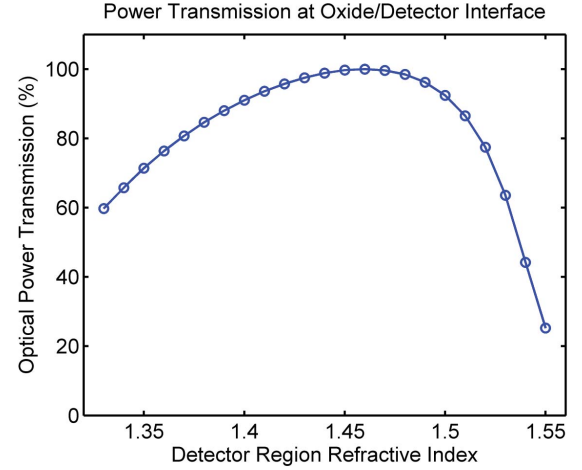


Fig. 6. Effect of refractive index mismatch on transmission at the reference/sensing region interface for $n = 1.46$ reference region.

predominately aqueous detector region ($n = 1.33$), the power transmission is only 60% . This power transmission effect has significant implications for device sensitivity.

Ideally, the refractive index of the reference region should be slightly lower than the anticipated refractive index range for the sensing region. For close index matching, nearly 100% of light will be transmitted; however there will still be an effect on the measured photocurrent in the sensing region, as the photocurrent in the sensing region is normalized with respect to photocurrent in the upstream reference region, such that $I_{normalized} = I_{sensing} / I_{reference}$.

If the reference region has a lower refractive index, the transmission effect can be exploited as a second sensing mechanism to work in concert with the local evanescent field shift mechanism. For example, as the refractive index of the sensing region is increased, the measured photocurrent would decrease as a result of less optical power transmission into the region and the evanescent field shift effect.

In contrast, if the reference region has a higher refractive index than the effective bulk index of the sensing region, the transmission effect and field shifting effect would work in opposite directions, obfuscating measurement, as the former would increase photocurrent and the latter would decrease photocurrent. For the proof of concept experiment discussed in Section IV, a reference region with refractive index slightly lower than the analyte was employed to take advantage of the dual sensing mechanisms (field shifting and transmission). For aqueous experiments, spin-on polymers such as Teflon AF ($n = 1.315$) (Dupont, Wilmington, DE) could be used to pattern reference regions of similar refractive index. It is worthwhile to note that a third sensing mechanism is present in the device. As the refractive index of the sensing region increases, scattering loss, which is proportion to Δn^2 will also decrease [24], further contributing to a decrease in photocurrent.

B. Fabrication Process for Waveguide Optimization

In an ideal LEAC device, propagation losses would solely result from the optical signal, namely photodetector coupling

losses modulated by changes in the sensing region upper cladding. However, both material properties and fabrication tolerances introduce absorption and scattering losses, which adversely affect sensor performance. Scattering and absorption decrease the signal to noise ratio by decreasing the intensity of the guided mode, which contributes to both shot-noise and quantization noise. Scattering is particularly detrimental, as scattered light incident on an integrated photodetector confounds measurement of the optical signal, i.e. the magnitude of photodetector coupling loss. It is essential to note that processing was done manually at a university lab using contact photolithography and not on a state-of-the-art commercial processing line. As such, feature resolution was limited to approximately 800 nm, which is substantially larger than the 22 nm processing capability currently used in commercial fabrication facilities [31]. Such coarse resolution can lead to significant sidewall roughness [32] and very high scattering losses. As such, processing and design steps were taken to minimize both absorption and scattering in the waveguide, subject to the processing capabilities of accessible fabrication equipment.

Absorption losses in PECVD oxide are negligible [26] however absorption losses in PECVD nitride can be significant. To minimize absorption losses, the PECVD nitride deposition technique first described by Gorin *et al.* was employed to deposit a highly transparent ($\alpha < 0.1$ dB/cm), low index ($n = 1.8$) SiN_x film. A loss of 0.1 dB/cm at 633 nm was reported for a nitride core planar waveguide [26] fabricated with minimally-absorbing PECVD nitride. As scattering losses are proportional to the square of the refractive index contrast (Δn^2) between the core and the cladding [30], the relatively low index nitride ($n = 1.8$ vs. $n = 2.1$) also has the beneficial effect of decreasing scattering losses relative to higher index nitride.

To further decrease scattering losses, the waveguide width w was increased to 7 μm versus 2 μm used in prior work [20]. In general, losses in ridge waveguides are inversely proportional to the fourth power of the largest guiding dimension [30], [33] (w for the LEAC waveguide structure). For a similar nitride core ridge waveguide structure with $H = 140$ nm, Bulla *et al.* reported a loss of 1 dB/cm for a $w = 5 \mu\text{m}$ versus 8 dB/cm for $w = 3 \mu\text{m}$ and concluded that the dominant scattering loss mechanism is sidewall roughness [30]. As waveguide width is increased, the losses asymptotically approach that of a planar waveguide. For our structure, vertical confinement is required. Waveguide propagation loss was evaluated on a test wafer with a thick 2.5 μm substrate to ensure negligible coupling losses for $w = 3$ to 10 μm , in increments of 1 μm (data not shown). The nitride core ($H = 30$ nm) was covered with 2 μm of oxide upper cladding. A 7 micron width was found to provide an optimal balance between scattering losses and insertion losses, which increase as w is increased for coupling with a 4 micron fiber. For $w = 7 \mu\text{m}$, losses of ~ 10 dB/cm were measured by analyzing CCD-acquired images of the attenuation of scattered light.

An analytical scattering loss model [34], first employed by Lee *et al.*, was adapted to the LEAC waveguide structure, in order to understand the effect of rms sidewall roughness σ

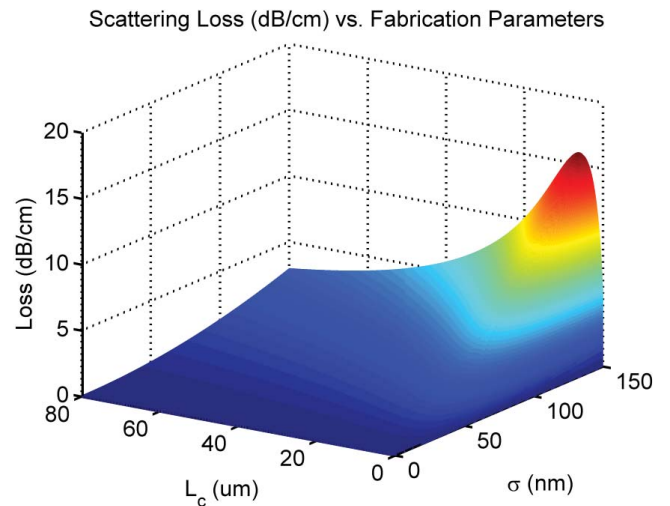


Fig. 7. Scattering loss as a function of rms sidewall roughness σ and autocorrelation length L_c for a 7- μm -wide LEAC waveguide.

and autocorrelation length L_c on scattering loss. The model assumes that scattering loss is dominated by sidewall roughness. Fig. 7 illustrates the effect of σ and L_c and scattering loss for a (7 $\mu\text{m} \times 30$ nm core) LEAC waveguide.

A measured waveguide loss of 10 dB/cm corresponds to a sidewall rms surface roughness of ~ 100 nm. For such a waveguide with $t_{\text{oxide}} = 1000$ nm, the magnitude of photodetector coupling loss to scattering loss is approximately unity for a 0.01 change in refractive index. It is worth mentioning that fabrication employing ultra-low-loss waveguides could significantly improve device performance by dramatically increasing the ratio of substrate coupling loss to scattering loss. Recently, Bauters *et al.* have demonstrated single-mode nitride waveguides using DUV lithography with $\sigma \sim 10$ nm and losses of just 0.001 dB/cm [35].

V. EXPERIMENT, RESULTS AND ANALYSIS

A. Photocurrent Measurements

For all experiments light is first end-fire fiber coupled into the waveguide with a fiber excited by a red laser diode centered about 650 nm as shown in Fig. 3b. A chip with a waveguide core height of 30 nm and a lower cladding thickness of 1000 nm was used. While the modesolver simulation results indicated that a chip with a waveguide core height of 30 nm and a 750 nm lower cladding would give better sensitivity, we were unable to couple a guided mode into chips fabricated with these dimensions, likely due to very high substrate coupling losses approaching 70 dB/cm.

The photocurrent at each detector $I_{\text{det},i}$ is measured at a sampling rate of 4 kHz using the circuit described in Section III. A probe card was used to probe the chip's metal output pads. Due to the high Schottky barrier produced by the Ti/Si contacts on the chip [24], [36], measured dark currents were uniformly small (~ 15 nA), and negligible compared to the measured photocurrent, which was on the order of 1–0.5 μA , depending on detector position. For consistency, the dark current at each detector was subtracted from the measured current, in order to compute the actual photocurrent.

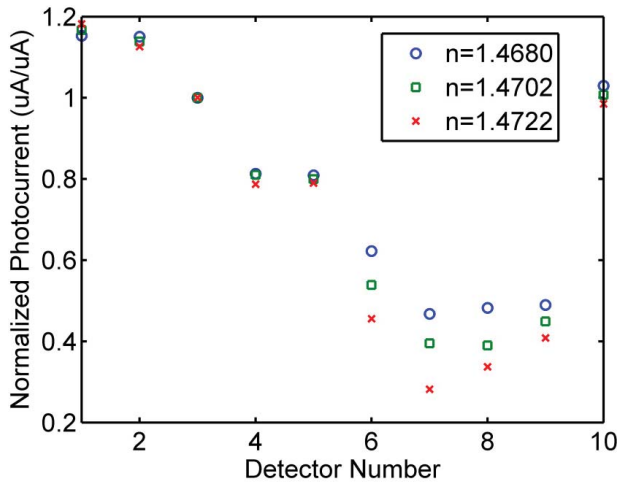


Fig. 8. Static refractive index sensing. In the reference region (detectors #1–5), the measured photocurrent is similar. In the sensing region (detectors #6–10), there is a dramatic difference in the measured photocurrent.

To normalize for fluctuations in coupled light intensity due to source instability and fiber movement, the photocurrent I_{ref} in the 3rd detector in the upstream reference region is measured immediately after each detector channel measurement, in order to calculate the normalized photocurrent of $I_{normalized,i} = I_{det,i}/I_{ref}$. Sesame oil, peanut oil, and a 50:50 sesame oil/peanut oil blend were used as fluids for the experiments. Both oils have negligible absorption at 650 nm, as measured by absorption spectrometry. The refractive indices of sesame ($n = 1.4722$), peanut ($n = 1.4680$), and blend ($n = 1.4702$) were measured using an Abbe refractometer. Both static and real-time measurements were performed.

B. Static Measurements

In the first experiment, each oil was injected into the fluidic channel; then flow was stopped and photocurrents were measured for 2 s on each channel. The purpose of this experiment was to determine the sensitivity of the device for a relatively long sampling time and observe photodetector coupling at different points along the waveguide. To improve signal to noise, photocurrent measurements were averaged over the 2 s acquisition time window. Results are shown in Fig 8.

C. Analysis of Static Measurements

As expected, the measured photocurrents in the reference region (detectors #1–5) are nearly identical, owing to the fixed upper cladding index. In the sensing region (detectors #6–#10), measured photocurrent increases as refractive index decreases, due to three sensing mechanisms: field shifting, transmission, and index-dependent scattering. The normalized photocurrent decreases due to scattering and photodetector coupling losses as light propagates down the waveguide. Without a prior calibration on each sensing detector using fluids of known refractive index, exact refractive index determination using the current device would be difficult, as there is not a precise relationship between the shift in photocurrent and change in refractive index on all detectors.

We attribute this behavior to two likely causes: localized scattering defects and slight deviations in photodetector response. First, localized scattering defects, observed as $\sim 1\mu\text{m}^2$ bright scattering spots along the excited waveguide would elevate the measured photocurrent in the corresponding detector region. Second, the photodetectors exhibited slight deviations ($\pm 5\%$) in photodetector response under uniform lamp illumination. These deviations would influence the measured photocurrent without a priori calibration on each detector.

Despite this shortcoming, the chip is very sensitive to small changes in refractive index. For analysis, Detector #7 is judiciously selected, as it provides the best sensitivity out of all detectors in the sensing region and was noted not to exhibit any localized scattering defect. It exhibits the greatest change in photocurrent (ΔI) for the fixed refractive index difference (ΔRIU) between sesame and peanut oil (0.0042). For 8000 photocurrent measurements over 2 s, the standard deviation of the normalized photocurrent was 0.006. This gives a photocurrent standard error ($SE_{\text{photocurrent}}$) of $0.006/\sqrt{8000} = 6.7 \times 10^{-5}$. The 95% confidence intervals for the uncertainty in photocurrent (δI) is then given by $3.92 \times (SE_{\text{photocurrent}}) = 2.63 \times 10^{-4}$. $\Delta \text{RIU}/\Delta I = 0.0176 \text{ RIU/normalized photocurrent unit}$. Assuming a linear photocurrent response, the minimal resolvable change in refractive index is then $(\Delta \text{RIU}/\Delta I)(\delta I) = 4.6 \times 10^{-6} \text{ RIU}$ for static measurements.

D. Real-Time Measurements

In the second proof of concept experiment, real-time measurements were performed by flowing oils into the fluidic chamber in the following order: sesame, blend, peanut, sesame. Photocurrent was measured on the second detector in the sensing region (#7) and normalized to the third detector in the reference region (#3). Oils were injected manually using a syringe in 20 s intervals and care was taken to strain relieve the tubes, in order to minimize coupling misalignment caused by fluid flow. Real-time refractive index sensing results are shown in Fig. 9.

E. Analysis of Real-Time Results

In a manner nearly identical to static measurements, the photocurrent increases as fluids of decreasing refractive index flow through the channel. Notably, the photocurrent returns to its initial value when sesame oil ($n = 1.4722$) once again flows through the channel. The data are significantly more noisy than the static measurements. The increased noise is likely caused by deviations in fiber coupling efficiency due to slight mechanical displacements caused by fluid flow in the channel. While the coupling is normalized by alternating sensing detector and reference detector photocurrent measurements, it was not normalized using simultaneous measurements due to limitations of our data acquisition system. The average standard error of the 10 data points for each flow period is 6×10^{-4} . Using a parallel analysis to the static measurements, described above, the minimum resolvable change in refractive index is 4.1×10^{-5} .

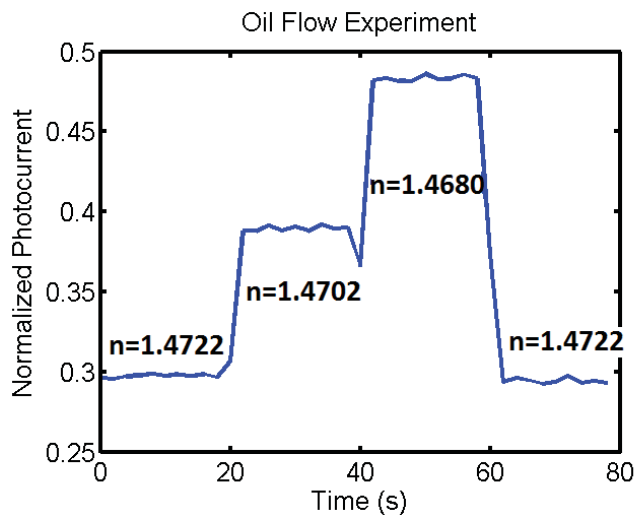


Fig. 9. Real-time refractive index sensing. Three fluids of known refractive index were flown through the chamber in 20-s intervals to validate the real-time sensing capabilities of the chip. As expected, the photocurrent is modulated by changes in the refractive index, and decreases as refractive index increases.

F. Comparison to Simulation Results

For the device fabricated, modesolver results predict $\Delta Loss = 17.49$ dB/cm for $n = 1.4680$ and 11.72 dB/cm for $n = 1.4722$, corresponding to fractional photodetector coupling losses of 0.040 and 0.026 over one detector, respectively. This gives a photodetector coupling ratio of 1.48, which is quite similar to the measured photocurrent ratio of 1.62 for $n = 1.4680$ vs. $n = 1.4722$ on detector #7. The improvement over the predicted value may be accounted for by the other two sensing mechanisms (transmission effect and scattering reduction) discussed previously.

VI. CONCLUSION

The LEAC biosensing chip has been optimized using results of a full-vector finite-difference modesolver. Device performance has been discussed within the context of fabrication tolerances. For the first time, the platform has been rigorously simulated and validated for both static and real-time fluidic measurements with an integrated fluidic channel, with minimal resolvable change in refractive index sensitivities of 4.6×10^{-6} and 4.1×10^{-5} , respectively. A robust continuous 1-D detector array has been implemented for localized photocurrent measurements. The utility of patterned on-chip reference regions have been experimentally validated and the refractive index requirements of the reference have been specified in the context of mode-matching to both ensure adequate light propagation down the waveguide and take advantage of the transmission sensing mechanism. These chip design improvements lay the groundwork for a fully portable biosensing chip with an integrated light source, which would enable multi-analyte detection if multiple reference and sensing regions were patterned onto a single waveguide. We anticipate that deep UV (DUV) lithography could be used to both further reduce waveguide scattering losses and permit the fabrication of a grating coupler [37], which would enable

waveguide coupling with a flip-chip laser [38]. These improvements would lead to the realization of a fully integrated optoelectronic CMOS-compatible biosensor requiring no external optical hardware.

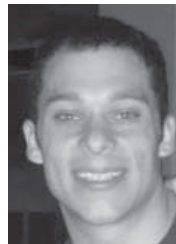
ACKNOWLEDGMENT

The authors would like to thank J. V. Zeghbrock, T. Borsa and many others at the Colorado Nanofabrication Lab (CNL) for sharing their fabrication expertise.

REFERENCES

- [1] M. Sumetsky, R. S. Windeler, Y. Dulashko, and X. Fan, "Optical liquid ring resonator," *Opt. Exp.*, vol. 15, no. 22, pp. 14376–14381, Oct. 2007.
- [2] K. D. Vos, I. Bartolozzi, E. Schaech, P. Bienstman, and R. Baets, "Silicon-on-Insulator microring resonator for sensitive and label-free biosensing," *Opt. Exp.*, vol. 15, no. 12, pp. 7610–7615, 2007.
- [3] M. Iqbal, M. A. Gleeson, B. Spaugh, F. Tybor, W. G. Gunn, M. Hochberg, T. Baehr-Jones, R. C. Bailey, and L. C. Gunn, "Label-free biosensor arrays based on silicon ring resonators and high-speed optical scanning instrumentation," *IEEE J. Sel. Topics Quantum Electron.*, vol. 16, no. 3, pp. 654–661, May–Jun. 2010.
- [4] D. Monzon-Hernandez and J. Villatoro, "High resolution refractive index sensing by means of a multiple-peak surface plasmon resonance optical fiber sensor," *Sens. Actuators B*, vol. 115, pp. 227–231, Nov. 2006.
- [5] R. Slavik and J. Homola, "Ultrahigh resolution long range surface plasmon-based sensor," *Sens. Actuators B*, vol. 123, no. 1, pp. 10–12, 2007.
- [6] P. Preechaburana, M. C. Gonzalez, A. Suska, and D. Filippini, "Surface plasmon resonance chemical sensing on cell phones," *Angew. Chem.*, vol. 51, no. 46, pp. 11585–11588, Nov. 2012.
- [7] Z. Tian, S. Yam, J. Barnes, W. Bock, P. Greig, J. Fraser, H. Looch, and R. Oleschuk, "Refractive index sensing with mach-zehnder interferometer based on concatenating two single-mode fiber tapers," *IEEE Photon. Technol. Lett.*, vol. 20, no. 8, pp. 626–628, Apr. 2008.
- [8] Z. Tian, S. Yam, and H. Looch, "Refractive index sensor based on an abrupt taper Michelson interferometer in a single-mode fiber," *Opt. Lett.*, vol. 33, no. 10, pp. 1105–1107, 2008.
- [9] B. Luff, J. Wilkinson, J. Piehler, U. Hollenbach, J. Ingenhoff, and N. Fabricius, "Integrated optical Mach-Zehnder biosensor," *J. Lightw. Technol.*, vol. 16, no. 4, pp. 583–592, Apr. 1998.
- [10] A. Crespi, Y. Gu, B. Ngamsom, H. J. Hoekstra, C. Dongre, M. Pollnau, and R. Osellame, "3-D Mach-Zehnder interferometer in a microfluidic chip for spatially-resolved label-free detection," *Lab Chip*, vol. 10, no. 9, pp. 1167–1173, 2010.
- [11] J. J. Lillie, M. A. Thomas, N. M. Jokerst, S. E. Ralph, K. A. Dennis, and C. L. Henderson, "Multimode interferometric sensors on silicon optimized for fully integrated complementary-metal-oxide-semiconductor chemical-biological sensor systems," *J. Opt. Soc. Amer. B*, vol. 23, no. 4, pp. 642–651, Apr. 2006.
- [12] A. Ymeti, J. S. Kanger, J. Greve, P. V. Lambeck, R. Wijn, and R. G. Heideman, "Realization of a multichannel integrated Young interferometer chemical sensor," *Appl. Opt.*, vol. 42, no. 28, pp. 5649–5660, 2003.
- [13] S. Mandal and D. Erickson, "Nanoscale optofluidic sensor arrays," *Opt. Exp.*, vol. 16, no. 3, pp. 1623–1631, 2008.
- [14] D. Wu, B. Kuhlmeier, and B. Eggleton, "Ultrasensitive photonic crystal fiber refractive index sensor," *Opt. Lett.*, vol. 34, no. 3, pp. 322–324, Feb. 2009.
- [15] A. Iadicicco, S. Campopiano, A. Cutolo, M. Giordano, and A. Cusano, "Refractive Index Sensor Based on Microstructure Fiber Bragg Grating," *IEEE Photon. Technol. Lett.*, vol. 17, no. 6, pp. 1250–1252, Jun. 2005.
- [16] Z. Ran, Y. Rao, W. Liu, X. Liao, and K. Chiang, "Laser-micromachined Fabry-Perot optical fiber tip sensor for high-resolution temperature-independent measurement of refractive index," *Opt. Exp.*, vol. 16, no. 3, pp. 2252–2263, 2007.
- [17] P. Yager, J. Domingo, and J. Gerdes, "Point of care diagnostics for global health," *Annu. Rev. Biomed. Eng.*, vol. 10, no. 3, pp. 107–144, Mar. 2008.
- [18] R. Yan and K. Lear, "Label-free silicon photonic biosensor with integrated detector array," *Lab Chip*, vol. 9, no. 15, pp. 2163–2168, 2009.
- [19] G. Yuan, K. Lear, M. Stephens, and D. Dandy, "Initial demonstration of a local, evanescent, array coupled biosensor concept," in *Proc. IEEE Sensors*, Oct.–Nov. 2005, pp. 908–910.

- [20] R. Yan, N. Lynn, L. Kingry, Z. Yi, R. Slayden, D. Dandy, and K. Lear, "Waveguide biosensor with integrated detector array for tuberculosis sensing," *Appl. Phys. Lett.*, vol. 98, no. 1, pp. 013702-1–013702-3, Jan. 2011.
- [21] R. Yan, G. Yuan, M. Stephens, X. He, C. Henry, D. Dandy, and K. Lear, "Evanescence field response to immunoassay layer thickness on planar waveguides," *Appl. Phys. Lett.*, vol. 93, no. 10, pp. 101110-1–101110-3, 2008.
- [22] A. Fallahkhair, K. Li, and T. Murphy, "Vector finite difference modesolver for anisotropic dielectric waveguides," *J. Lightw. Technol.*, vol. 26, no. 11, pp. 1423–1431, Jun. 2008.
- [23] W. Kern, "The evolution of silicon wafer cleaning technology," *J. Electrochem. Soc.*, vol. 137, no. 6, pp. 1887–1892, 1990.
- [24] R. Ohta, C. Viana, N. Morimoto, and B. Borges, "Fabrication of Ti-Si-Ti metal-semiconductor-metal photodetectors using low temperature rapid thermal annealing," *J. Integr. Circuits Syst.*, vol. 2, no.2, pp. 85–88, 2007.
- [25] J. Batey and E. Tierney, "Low-temperature deposition of high-quality silicon dioxide by plasma-enhanced chemical vapor deposition," *J. Appl. Phys.*, vol. 60, no. 9, pp. 3136–3144, 1986.
- [26] A. Gorin, A. Jaouad, E. Grondin, V. Aimez, and P. Charette, "Fabrication of silicon nitride waveguides for visible-light using PECVD: A study of the effect of plasma frequency on optical properties," *Opt. Exp.*, vol. 16, no. 18, pp. 13509–13516, 2008.
- [27] B. Bilenberg, T. Nielsen, B. Clausen, and A. Kristensen, "PMMA to SU-8 bonding for polymer based lab-on-a-chip systems with integrated optics," *J. Micromechan. Microeng.*, vol. 14, no. 6, pp. 814–818, 2004.
- [28] C. Cohn, "Plastic pin grid array package," U.S. Patent 5 102 829, Apr. 7, 1992.
- [29] A. Yariv, "Coupled-mode theory for guided-wave optics," *IEEE J. Quantum Electron.*, vol. 9, no. 9, pp. 919–933, Sep. 1973.
- [30] D. Bulla, B. Borges, M. Romero, N. Morimoto, L. Neto, and A. Cortes, "Design and fabrication of SiO₂/Si₃N₄ CVD optical waveguides," in *Proc. SBMO/IEEE MTT-S, APS, LEOS, Int. Microw. Optoelectron. Conf.*, vol. 2, Aug. 1999, pp. 454–457.
- [31] H. Iwai, "Roadmap for 22 nm and beyond," *Microelectron. Eng.*, vol. 86, no. 7–9, pp. 1520–1528, 2009.
- [32] R. W. Hunsperger, *Integrated Optics: Theory and Technology*. Berlin, Germany: Springer-Verlag, 1984.
- [33] F. Payne and J. Lacey, "A theoretical analysis of scattering loss from planar optical waveguides," *Opt. Quantum Electron.*, vol. 26, no. 10, pp. 977–986, Oct. 1994.
- [34] K. Lee, D. Lim, H. Luan, A. Agarwai, J. Foresi, and L. Kimerling, "Effect of size and roughness on light transmission in a Si/SiO₂ waveguide: Experiments and model," *Appl. Phys. Lett.*, vol. 77, no. 11, pp. 1617–1619, 2000.
- [35] J. Bauters, M. Heck, D. John, D. Dai, M. Tien, J. Barton, A. Leinse, R. Heideman, D. Blumenthal, and J. Bowers, "Ultra-low-loss high-aspect-ratio Si₃N₄ waveguides," *Opt. Exp.*, vol. 19, no. 4, pp. 3163–3174, 2011.
- [36] R. P. MacDonald, N. G. Tarr, B. A. Syrett, S. A. Boothroyd, and J. Chrostowski, "MSM photodetector fabricated on polycrystalline silicon," *IEEE Photon. Technol. Lett.*, vol. 11, no. 1, pp. 108–110, Jan. 1999.
- [37] P. Dumon, W. Bogaerts, V. Wiaux, J. Wouters, S. Beckx, J. Van Campenhout, D. Taillaert, B. Luyssaert, P. Bienstman, D. Van Thourhout, and R. Baets, "Low-loss SOI photonic wires and ring resonators fabricated with deep UV lithography," *IEEE Photon. Technol. Lett.*, vol. 16, no. 5, pp. 1328–1330, May 2004.
- [38] C. Liu, Y. Lin, M. Houg, and Y. Wang, "The microstructure investigation of flip-chip laser diode bonding on silicon substrate by using indium-gold solder," *IEEE Trans. Compon. Packag. Technol.*, vol. 26, no. 3, pp. 635–641, Sep. 2003.



Tim A. Erickson (S'11) received the M.S. degree in biomedical engineering from the University of Texas at Austin, Austin, TX, USA, in 2009. He is currently pursuing the Ph.D. degree in electrical engineering under the guidance of Dr. Kevin Lear at Colorado State University, Fort Collins, CO, USA.

His current research interests include design of portable sensing platforms for environmental monitoring and medical diagnostics.



Kevin L. Lear (M'90) is a Professor of Electrical and Computer Engineering and Associate Director of the School of Biomedical Engineering with Colorado State University, Fort Collins, CO, USA.

His research interests include optoelectronics, portable biosensors, and vertical-cavity surface-emitting lasers.